6th International Symposium on Solid Mechanics

Click on the box to select the Mini-Symposia:

☐ Multiaxial and Fretting Fatigue (*Edgar Mamiya* and *Lucival Malcher*);

☐ Composite Materials (*Ricardo de Medeiros*);

☒ Constitutive Models I – Plasticity and Damage (*Lucival Malcher*, *Miguel Vaz Jr.* and *Edgar Mamiya*);

☐ Constitutive Models II – Viscoelastic and Viscoplastic Solids: Models and Applications (*Heraldo Mattos*);

☐ Impact Engineering (*Marcílio Alves*);

☐ Structural Reliability Methods and Reliability-Based Design Optimization (*André Beck*);

☐ Topology Optimization of Multifunctional Materials, Fluids and Structures (*Eduardo Lenz Cardoso* e *Emilio Carlos Nelli Silva*);

☐ Topological Derivatives: Theory and Applications (*André Novotny*);

☒ X-FEM, G-FEM and Meshfree Methods (*Roberto Dalledone Machado* and *Rodrigo Rossi*);

☐ High Order Finite Elements (*Marco Lúcio Bittencourt*);

☐ Nonlinear Analyses (*Eduardo Campello*);

☐ Other section;

MECSOL Joinville 2017

April 26-28, 2017
Joinville, Santa Catarina, Brazil

FINITE ELEMENT ANALYSIS OF THE LAMB WAVES BEHAVIOR ON THE LEADING EDGE OF WINGS AND WIND TURBINE BLADES MADE OF COMPOSITES

Guilherme André Santana
Departamento de Engenharia de Estruturas (DEES)
Universidade Federal de Minas Gerais (UFMG) – Belo Horizonte – MG - Brazil
guilhermeandresantana@gmail.com

Mohammad Malekan
Departamento de Engenharia de Estruturas (DEES)
Universidade Federal de Minas Gerais (UFMG) – Belo Horizonte – MG - Brazil
mmalekan1986@gmail.com

Lázaro Valentim Donadon
Departamento de Engenharia Mecânica (DEMEC)
Universidade Federal de Minas Gerais (UFMG) – Belo Horizonte – MG - Brazil
lazaro@demec.ufmg.br

Alexandre Martins Araújo
Departamento de Engenharia Mecânica (DEMEC)
Universidade Federal de Minas Gerais (UFMG) – Belo Horizonte – MG - Brazil
alemartins93@hotmail.com

Carlos Alberto Cimini Jr.
Departamento de Engenharia de Estruturas (DEES)
Universidade Federal de Minas Gerais (UFMG) – Belo Horizonte – MG - Brazil
Carlos.cimini@gmail.com

ABSTRACT

The behavior of Lamb Waves (Surface Waves) for thin composite plates is well known. The underlying physics of these waves are being used in the field of Structural Health Monitoring, to access the existence, the location and the size of damages on aerospace and composite structures overall, including wind turbine blades. However, no thorough study was made regarding the effect of the high curvature to thickness ration in the leading edge of those structures. This characteristic changes the Lamb Waves and, hence, the algorithms for accessing damage need to account for that. This work shows the expected changes on the Lamb Waves for specific glass fiber reinforced polymer skins for many values of curvature to thickness on the leading edge, showing trends that can be used on future modifications of the algorithm for structural health monitoring of those structures. This study is done through finite element method using a dynamic explicit analysis of orthotropic constitutive model and continuum shell elements, using an automated macro of an ABAQUS model, generating trends of speed change versus curvature to thickness ratio. It is shown that the analysis for high curvature skins changes considerably from the analysis of plates (plane skins), for values of curvature common for modern airfoils.

Keywords: SHM, wind turbine blades, wing, curvature

1 INTRODUCTION

Composite structures are continually more present on the today's structures. This type of structure was mainly used in the aerospace/marine industries and among other exotic areas until the 1980s, like high end automobile industry and professional sporting goods (e.g. bike frames, golf rackets). But since the 1990s, the wind energy industry started to gain momentum and is now one of the main worldwide users of composite materials [1].

Most Wind turbine blades (WTB) have a structure that resemble a two or three cell aircraft wing. The skin is normally made of bidirectional glass fiber reinforced polymer (GFRP-epoxy) in a sandwich structure with PVC or light wood (e.g. balsa) and the main spar normally made from unidirectional carbon fiber reinforced polymer (CFRP-epoxy), as can be depicted from figure 1 below. These WTB can have as much as 75 meters span each and the trend of size is increasing [1]. These WTB behave aerodynamically like an aircraft wing, only it is rotating and have different airspeeds in function of the section position in the blade radius.

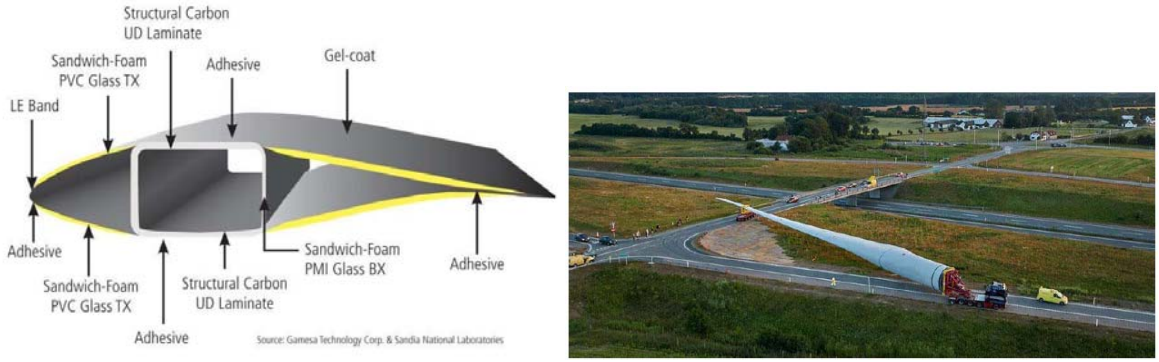

Figure 1 – Structure of wind turbine blade [2].

To provide a continuous and robust growth of this type of energy generation, the International Energy Agency set some goals and roadmaps in 2013 [1]. It was appointed by the agency that one of the main drawbacks of this type of energy generation was the operation and maintenance (O&M). According to the agency it is needed to improve diagnostic methods and preventive maintenance and wind plant data management in order to reduce costs, especially for off shore operations where access for the structure by the maintenance team can be difficult and expensive. Availability (proportion of the time that it is technically ready for usage) need to increase from the actual 90% average to 98%. To do that, less schedule maintenance and more predictive maintenance with intelligent sensors need to be used.

The WTB have many failure modes and the aftermath of those failures are most of the times catastrophic for the structure. There are many reported problems suffered by the skin of the WTB in the literature. Among them, it is possible to have: blade torsion overload and failure, impact induced delamination, leading edge erosion due to water droplets, ice formation on leading edges, trailing edge debonding due to excessive water absorption, lightning strike problems [3, 4].

A research have been initiated at the DEES/UFMG (*Departamento de Engenharia de Estruturas* – Structural Engineering Department) together with GRAVI/UFMG (*Grupo de acústica e vibrações* – Acoustics and Vibrations Group), in order to access the field of predictive maintenance

for WTB. That research is using Structural Health Monitoring (SHM) technique to access the damage on these structures.

The objectives of a complete SHM scheme nowadays can be described into six steps: i) identify the existence of damages; ii) identify the number of damages; iii) finding the damages location; iv) obtain the size of the damages; v) identify the probable type of damages and vi) access the hazard of the structure in real-time, through interpretation of the other steps.

A study done by the American Air Force showed that, with SHM, it was possible to disregard periodic structural inspections on aircraft, increasing aircraft availability from 88% to 98%. One might think that this generated a rather riskier and more failure prone situation, but what happened was quite the contrary. The MTBF (Mean Time Between Failure) went from 860 hours to 12800 hours [5], which is an indication of a much more reliable operation of the fleet.

The most used method of automatic sensor inspection used on aircraft structures is the Lamb Wave (LW) inspection. This field of SHM is commonly addressed as LW-SHM. Lamb Waves are surface mechanical waves that propagate on thin plates or curved skins. The mathematical treatment of such waves was discovered by Horace Lamb in 1914 [6]. To perform the LW-SHM, it is normally used piezoelectric actuators (PZT) bonded on the surface to generate the Lamb waves and PZT sensors to measure the waves in a matrix of sensors. Comparing a baseline signal (undamaged) with the damaged signal, it is possible to do the six steps of SHM described above through many different algorithms in the literature [7, 8, 9, 10].

There are many studies regarding LW-SHM in flat plates, for both isotropic or orthotropic materials for damage assessment. But, according to authors' knowledge, there are no studies about the effects of the leading edge curvature radius on the lamb waves behavior. That is more of an issue as the blades become more aerodynamically efficient, as very efficient airfoils tend to have big leading edge curvature (small radius). As many of the possible damages happen in the leading edge, it is important to access the change of Lamb Wave characteristics and, thus, improve the damage detection and assessment.

This work aims at finding these changes in Lamb Wave characteristics with curvature, using Finite Elements Analysis (FEA).

2 LAMB WAVES

The Lamb Waves are highly dispersive (speed changes with wave frequency) surface waves composed of two mode types: the symmetrical (S) and asymmetrical (A) modes. The direction of propagation of both modes are radially from a source. The S mode happens when the vibration is in the same direction as the wave propagation, they are longitudinal extension-contraction waves and are normally of lesser amplitude. The A mode happens when the vibration direction is perpendicular to the propagation direction and the surface, they are flexural waves and are normally of bigger amplitude. The first harmonic is numbered 0, the second is numbered 1 and so forth, such that S1 is the second symmetrical mode and A0 is the first asymmetrical mode, for example. There is also a wave that propagates radially, vibrates perpendicular to the propagation direction but is on the plane, it is the shear wave (SH). The last is not considered a Lamb Wave but it is common to see them together with the other modes on the dispersion curves. Figure 2 below shows the group velocities (C_g) of the many modes versus excitation frequency for a specific CFRP plate [11] (dispersion curves). The group velocity is the velocity of the modulation or "envelope" of the wave.

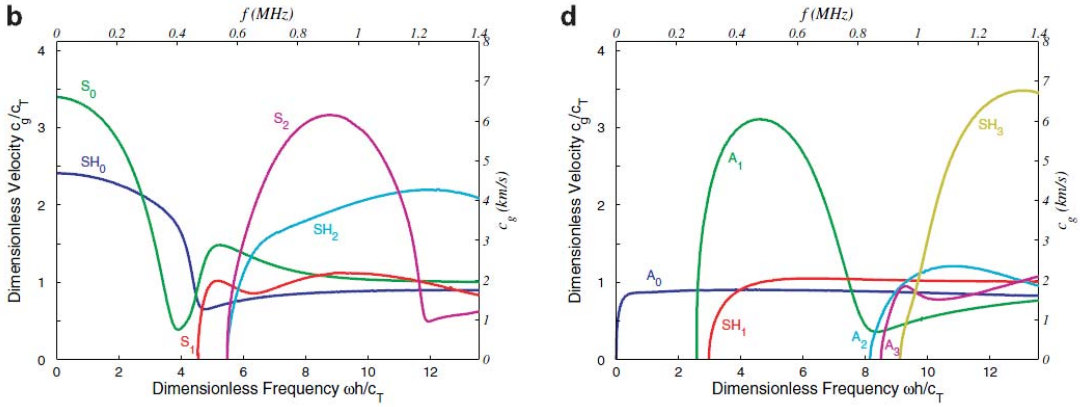

Figure 2 – Group velocity dispersion curves of $[+45_6/-45_6]_s$ laminate in 30º direction [11].

It is also possible to see the dimensionless velocity and dimensionless frequency in the parallel axis, function of "h", plate thickness, and C_T, the transverse shear wave velocity of the material. Using the dimensionless velocity and dimensionless frequency, those curves can be extrapolated to other materials and plate thicknesses for a first assessment of the Lamb waves. C_T can be calculated as:

$$C_T = \sqrt{\frac{G_{12}}{\rho}}; \tag{1}$$

where G_{12} is the shear modulus in the plane perpendicular to a fiber direction and acting perpendicular to the fiber and ρ is the laminate density.

It can be seen from figure 2 that in 100 kHz, for example, modes S0, A0 and SH0 are present, with the group velocities being 6.5 km/s, 2 km/s and 4.8 km/s respectively.

3 METHODOLOGY

This work deals specifically in trying to access the skin curvature influence in the group velocity of the Lamb waves with the usage of a linear dynamic explicit finite element simulation. The explicit method is a regular time marching algorithm that integrates the elastic equations over time, considering the mass and acceleration on the formulation. For each time increment, the next state is calculated from the previous states by numerical integration of the differential equations and by the load function. A fixed time increment was chosen to better control the simulation parameters and for better comparison between different simulation cases.

3.1 Excitation Frequency

The chosen excitation frequency was 50 kHz, which according to [9] is a good excitation frequency for SHM analysis. This frequency is small enough to decrease sampling time of real life applications and still has a good response of the A0 and S0 modes. In our case, the total simulation time is directly proportional to the excitation frequency for the same precision of results, hence, choosing smaller frequencies is important. For precision purposes, a sine wave needs to have at least 50 partitions, hence, the maximum allowed time increment of the simulation is chosen equal to 4e-7 seconds for 50 kHz excitation frequency.

3.2 Material properties

The structure material is E-glass fiber and epoxy matrix. The lamina stiffness properties were taken from [12] for normalized 60% fiber volume fraction. It is known from our laboratory practice that the maximum fiber volume fraction that can be achieved in the lab via vacuum bag and hand layup is 42% with fiberglass. Hence, every material property that is fiber dominated was multiplied by the ratio of 42/60. The final lamina properties can be seen in Table 1.

Table 1 – E-glass/epoxy material properties.

Lamina		
E1	2.90E+10	Pa
E2	6.39E+09	Pa
G12	2.82E+09	Pa
nu12	0.28	-
nu21	0.06	-
thickness	0.12	mm
Density	1506	Kg/m^3
Epoxy Ly5052		
E	3.30E+09	Pa
nu	0.35	-
G	1.22E+09	Pa

The Epoxy properties are important for the matrix dominated inputs, like G23.

It was decided that all plates would have 5 plies of the bidirectional plain weave fiberglass, i.e. $[-45/+45]_5$, (10 laminas, 5 on 45 degrees relating to the vertical and 5 on -45 degrees) yielding approximately 1.2 mm total plate thickness (value of "h" in figure 2). This is an approximate thickness because the curvature of the fibers in the weave is not considered. But this is a normal practice in the field and normally it is within the acceptable tolerances. No dissipation effects or internal damping was considered for this study.

3.3 Estimate of wave speeds and CFL condition

In order to access the total simulation time, it was used reference [11] dispersion curves depicted in figure 2. The determined S0 mode group velocity was approximately 4200 m/s and the group velocity of the A0 mode was approximately 1000 m/s. Propagation distances of 80 mm and 150 mm were chosen for the simulations until 8 mm radius of leading edge and for 50 mm radius, respectively. Hence, for the first group, the total time for the slower wave group to reach the target was 8e-5 s. The time it take for 5 Sine peaks to pass the receptor point was calculated as 1e-4. Thus, the total simulation time was considered equal to 18e-5 s.

An important feature must be considered for dynamic explicit analysis of waves using numerical methods. The wave must not travel more than the element length during a single time increment; otherwise, the results are going to be wrong and the simulation could be unstable. This is known as the Courant-Friedrichs-Lewy condition (CFL) [13]. The following inequality needs to be hold during the whole analysis:

$$\frac{u\Delta t}{L} \leq C_{\max}; \tag{2}$$

where "u" is the wave velocity, "Δt" is the time increment, "L" is the element length and "C_{max}" is the CFL criteria, which can hold a maximum of 1 for explicit methods. It was chosen C_{max} equal 0.5 for better stability. Hence, for a given time increment, we have a minimum element length that is considered stable. In order to decrease this element length for simulation accuracy, it is needed to decrease also the time increment in the same proportion.

The needed element length was accessed by geometry constraints. A maximum curvature tolerance factor of "h/L" of 0.01 was considered here, where "h" is the maximum distance from the arc to the element edge and "L" is the length of the element. For this condition, knowing that the element length would be the same for every radius in the simulations, the L was chosen based on the smaller simulated radius of 2 mm (critical case). Therefore, the chosen element size "L" was 0.3 mm.

Now, to attend the CFL condition, the time increment should not be more than:

$$\Delta t \leq \frac{C_{\max} \cdot L}{u} = \frac{0.5 \cdot 3e-4}{4.2e3} = 3.5e-8 \ s. \tag{3}$$

The value of time increment determined above is smaller than 10% of the maximum limit determined in section 3.1, so that it is suitable for usage and increased the resolution of the Sine wave.

3.4 Geometry generation of the part

The geometry to be simulated is a solid generated from an extrude from the sketch that can be seen in figure 3 below, together with the parameters that define it.

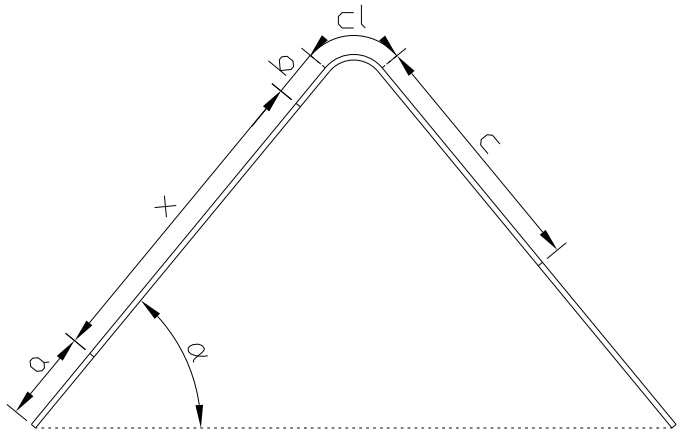

Figure 3 – Geometry of the part.

The determined parameters from 2 to 8 mm radius and 50 mm radius are listed in table 2 below:

Table 2 – Geometric parameters.

Radius (mm)	x (m)	a (m)	b (m)	c (m)	CL (m)	α (deg)
2	0.080	0.020	0.010	0.0664	0.0036	51.5
3	0.080	0.020	0.010	0.0645	0.0055	52.1
4	0.080	0.020	0.010	0.0627	0.0073	52.6
5	0.080	0.020	0.010	0.0607	0.0093	53.1
6	0.080	0.020	0.010	0.0588	0.0112	53.7
7	0.080	0.020	0.010	0.0568	0.0132	54.2
8	0.080	0.020	0.010	0.0547	0.0153	54.8
50	0.150	0.040	0.010	0.0206	0.1194	68.4

Partition lines where created in the coordinates of the source point and the receptor points, both in the plain part (hereby called plain receptor) and the one in which the wave passes through the curved part (hereby called curved receptor). Another partition line was created with the part mid plane, splitting the part in two. Figure 4 below depicts the partition lines, the source point and the receptor points, as well as the global frame of reference and its x (red arrow), y (green arrow) and z axis. It also shows the ply directions.

3.5 Element type and properties

The element type was the Abaqus® continuum shell linear hexahedral element with reduced integration, SC8R. This have 8 nodes with 3 translational degrees of freedom each. It was used the composite property to form the laminate, with the option solid composite. In order to set the ply

direction, it was used the option “discrete orientation” so that the x axis always accompany the curvature of the plate (always perpendicular to the normal vector) and is parallel to the lateral sketch of the plate.

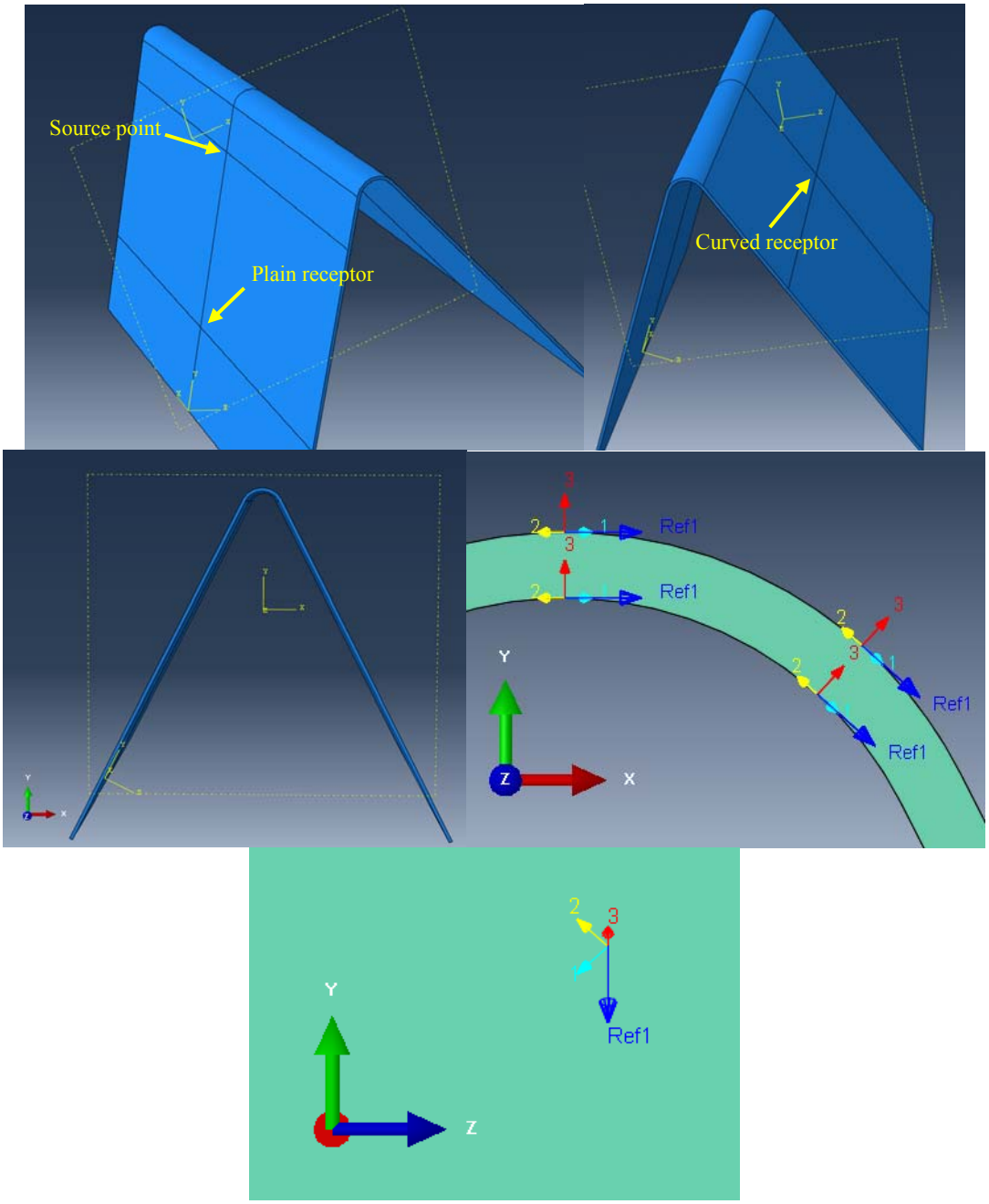

Figure 4 – Source, receptor points and ply direction.

3.6 Output characteristics

The recording of the simulation data was done creating two history outputs (two receptor points) and a field output. The two history outputs were the x, y and z displacements and were recorded for every simulation increment. After the simulation, it was generated a function that is the vector sum of the Ux (x axes displacement) and Uy (y axes displacement) displacements over time, to get the resultant displacement in the xy plane (Uxy).

The field outputs were the x, y and z displacements for every node and were recorded at every 12 increments. That was done to reduce the total volume of data to be recorded, but still being able to generate a smooth animation of the simulation.

3.7 Boundary Conditions

For simplicity sake, it was pinned 3 points in the extremities of the plates. The part of the wave that is going to be analyzed is mostly the beginning of the wave in the receptor points. Hence, the reflection of the wave happens some time after the instant of interest and the type of boundary condition makes no difference for the purposes of this work. That is because we are dealing with hyperbolic differential equations, so that it takes time for the deformation to reach close to the boundary condition and the effect of the boundary condition (reaction forces and reflection) to be felt.

3.8 Load

It was used a sin function with 50 kHz frequency and 0.1 N amplitude at the source point, acting perpendicular to the initial state of the plate.

4 RESULTS AND DISCUSSION

4.1 Field Output Results

Figures 5 until 9 below show the resultant displacement (x, y and z vector sum) over 5 different instants. All results are in the SI system. The geometric magnification scale of the displacement in the figures is 3.42e6, automatic determined by Abaqus® for clarity of view. The limits of the colormap of displacement were set from 0 m to 3.834e-11 m manually, so that it was possible to see the S0 wave by the colors. Those waves have almost 100 times smaller amplitude then the A0 waves and the figure would become too distorted in order to see S0 geometrically rather than on colors. All areas that have displacements bigger than 3.834e-11 m are represented with the gray color (saturation of the colormap).

It is possible to see that the S0 wave propagates more on a square pattern, with the 45 degrees direction approximately 20% bigger than the 0 direction. The A0 wave front in the +-45 degree direction have a propagation speed 14% bigger than in the 0 degrees direction. That happens because the orientation of the fibers are +45/-45 degrees (orthotropy) and similar patterns are found in the literature [11]. Also, the amplitudes of the S0 waves are much bigger in the +45/-45 than in the 0 degrees direction (0 degrees go until light green, whereas 45 degrees saturates on gray). Hence, the SHM algorithms that rely on amplitude variation to identify damage would suffer more from this feature. Clearly, the SHM algorithms that rely on time of flight (almost every one) with the S0 wave,

need to account for the wave propagation direction, for this type of laminate, otherwise big errors can occur.

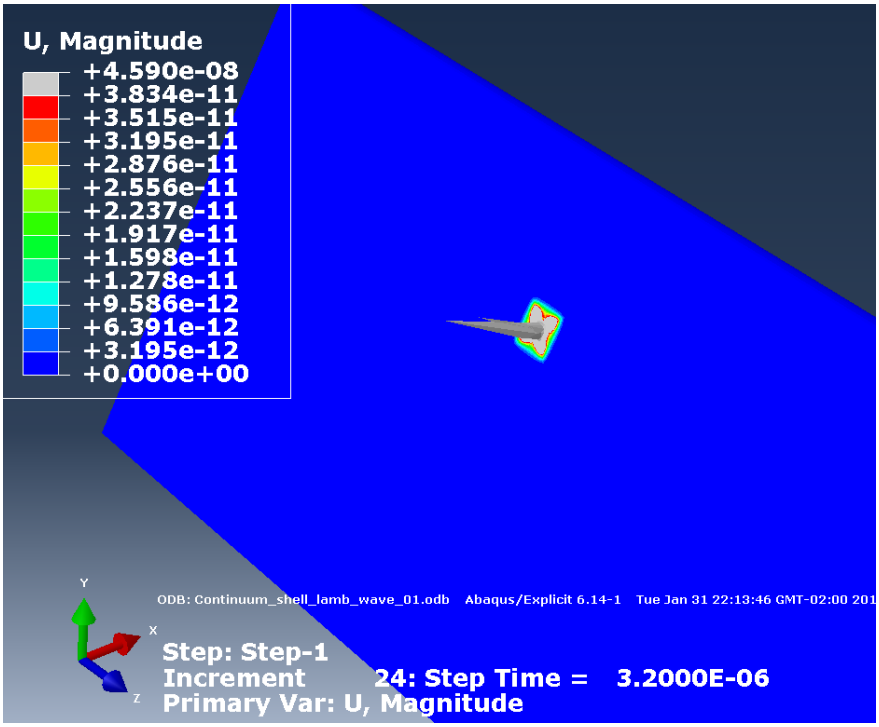

Figure 5 – Total real time of 3.2e-6.

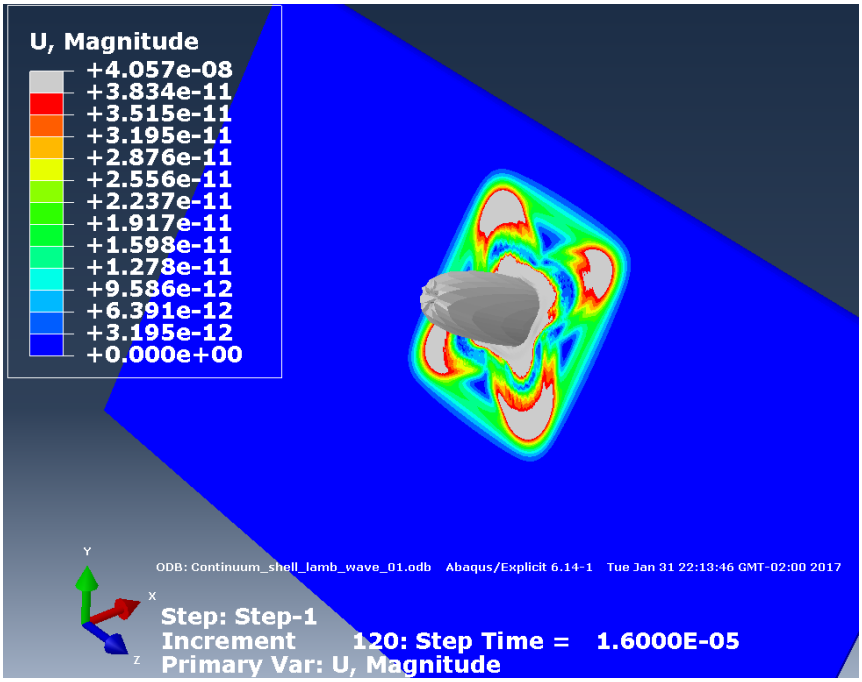

Figure 6 – Total real time of 1.6e-5.

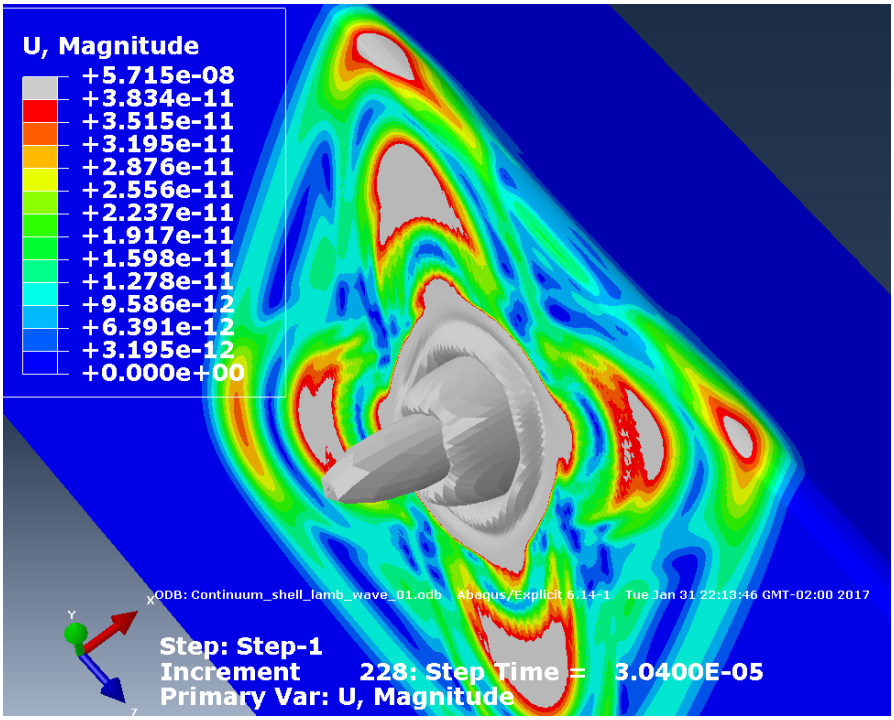

Figure 7 – Total real time of 3.04e-5 s.

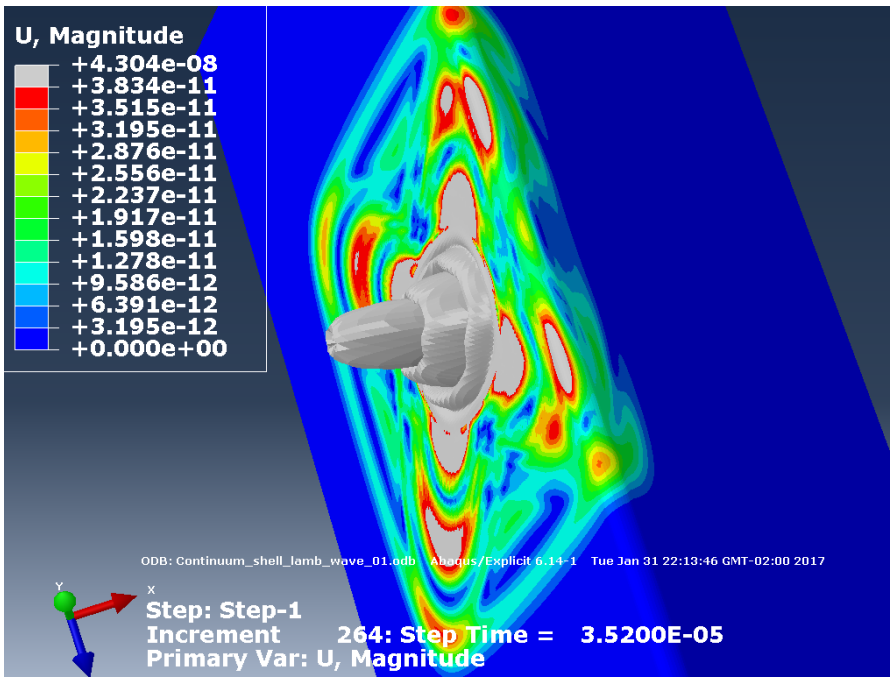

Figure 8 – Total time of 3.52e-5 s.

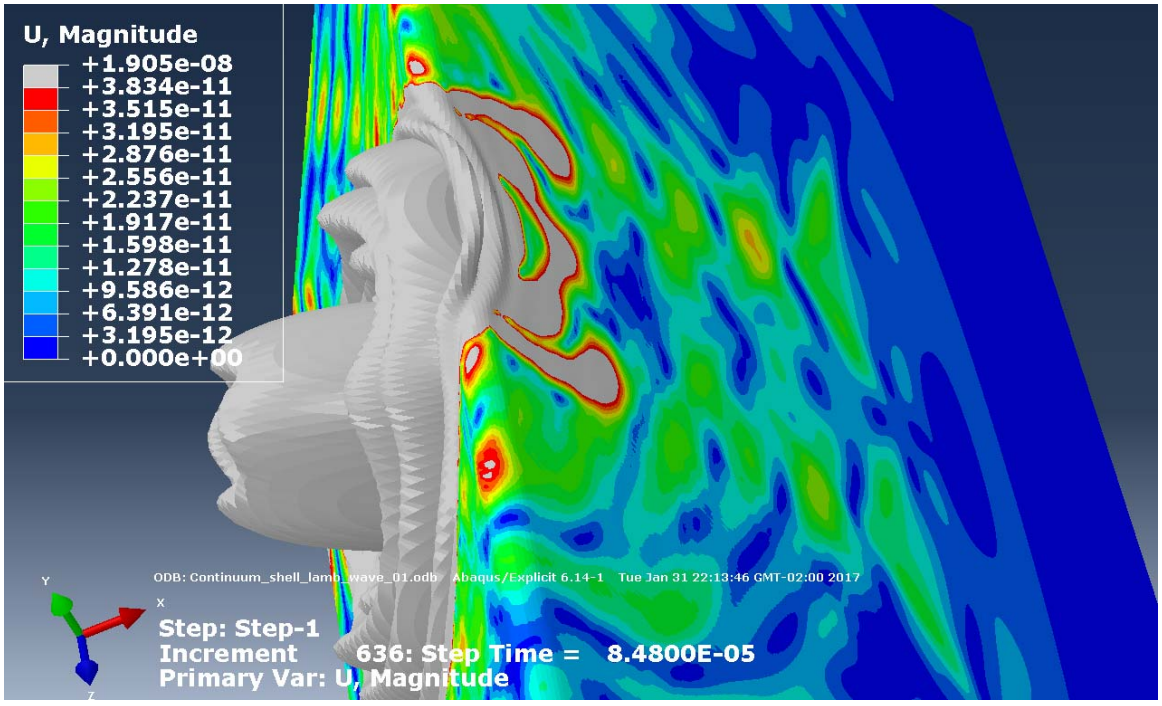

Figure 9 – Total real time of 8.48e-5 s.

Comparing the wave fronts between arrow “A” in figure 10 and arrow “B” in figure 11, it is possible to visualize a deflection of the wave front. That is a qualitative evidence of refraction in the leading edge (curved part), which is a change of the wave propagation speed.

4.2 History output results

The history output results showing the S0 mode first peak can be seen in the figures 12 and 13 below. It is possible to see that the time for which the peak is achieved increases with the radius of the leading edge. Also, the amplitude of the first peak increases with the leading edge radius.

The history output showing the A0 mode can be seen in figure 14. It wasn´t obvious to inspect as the S0 mode, possibly because of the interference of some of the reflected S0 wave in the total amplitude. But peaking the highest value between the first 3 peaks, it is possible to see a trend for some of the simulated radiuses. It is possible to see that the time of the peak also increases with the radius. However, for the A0 wave, the peak amplitude now decreases with the radius.

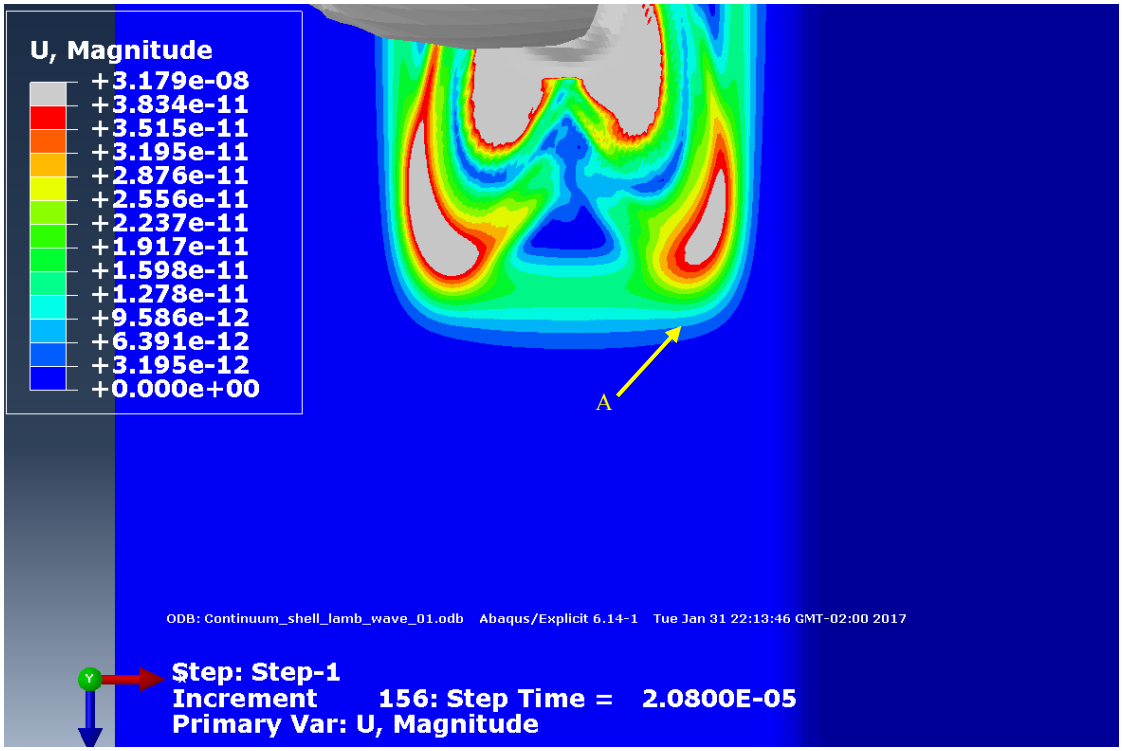

Figure 10 – Superior view without perspective (2.08e-5 s).

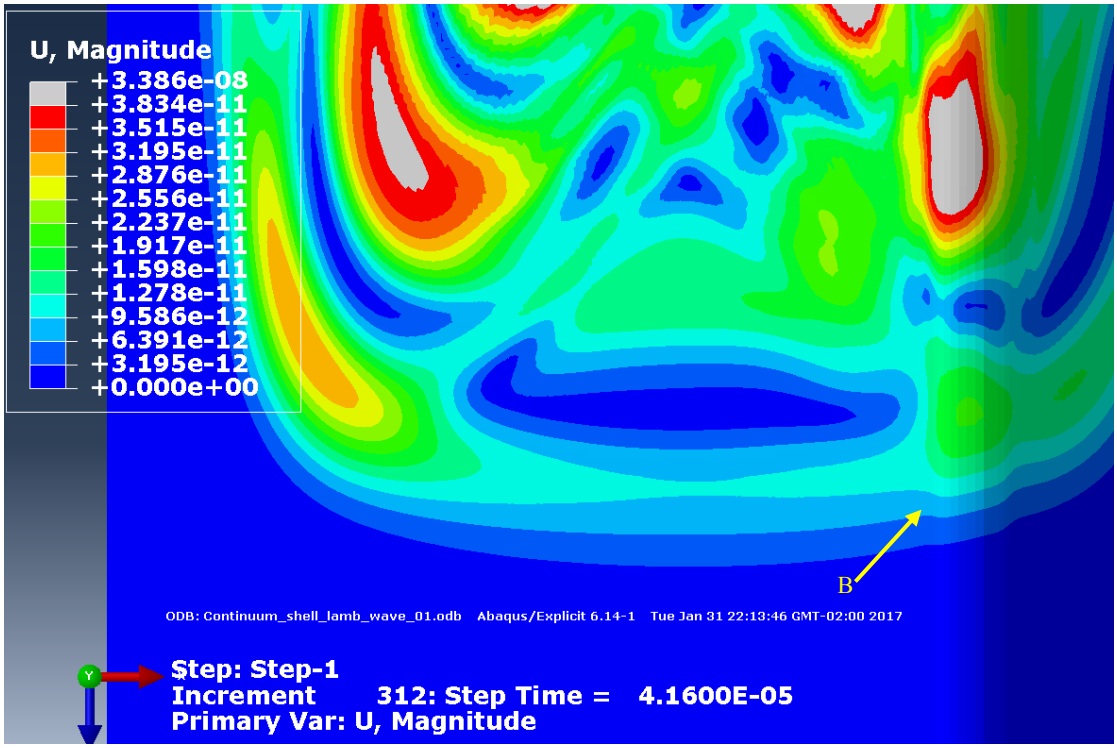

Figure 11 – Superior view without perspective (4.16e-5 s).

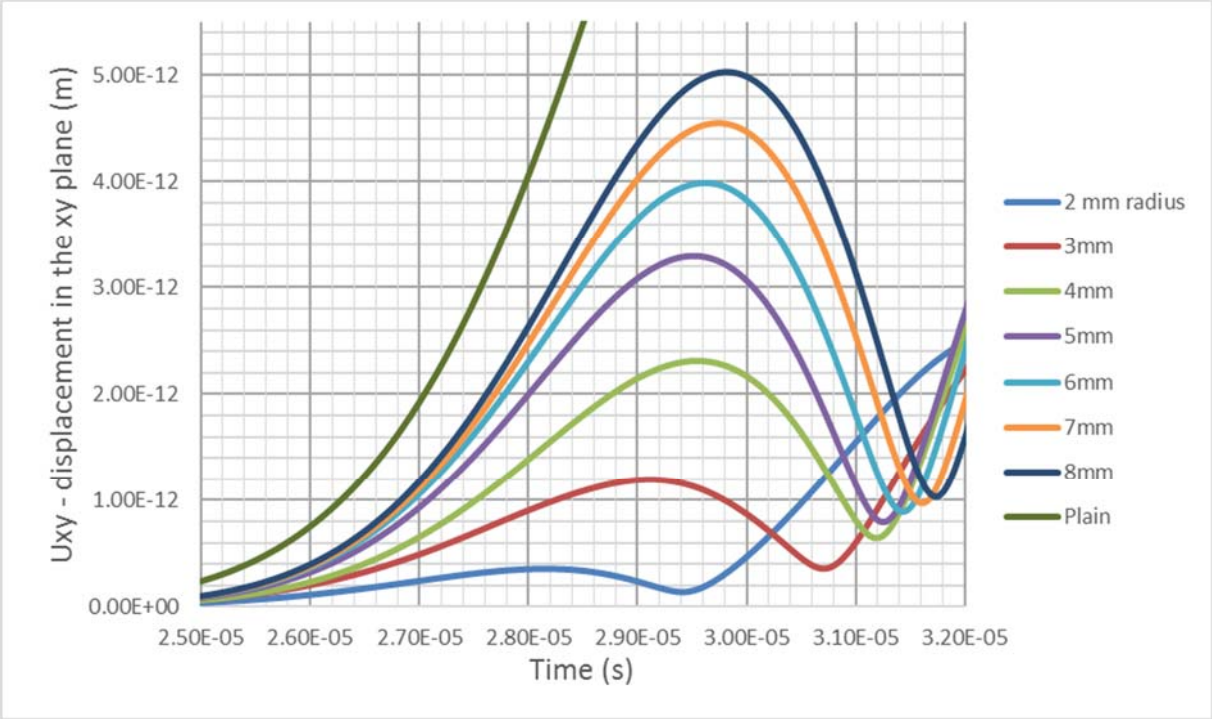

Figure 12 – First S0 wave front.

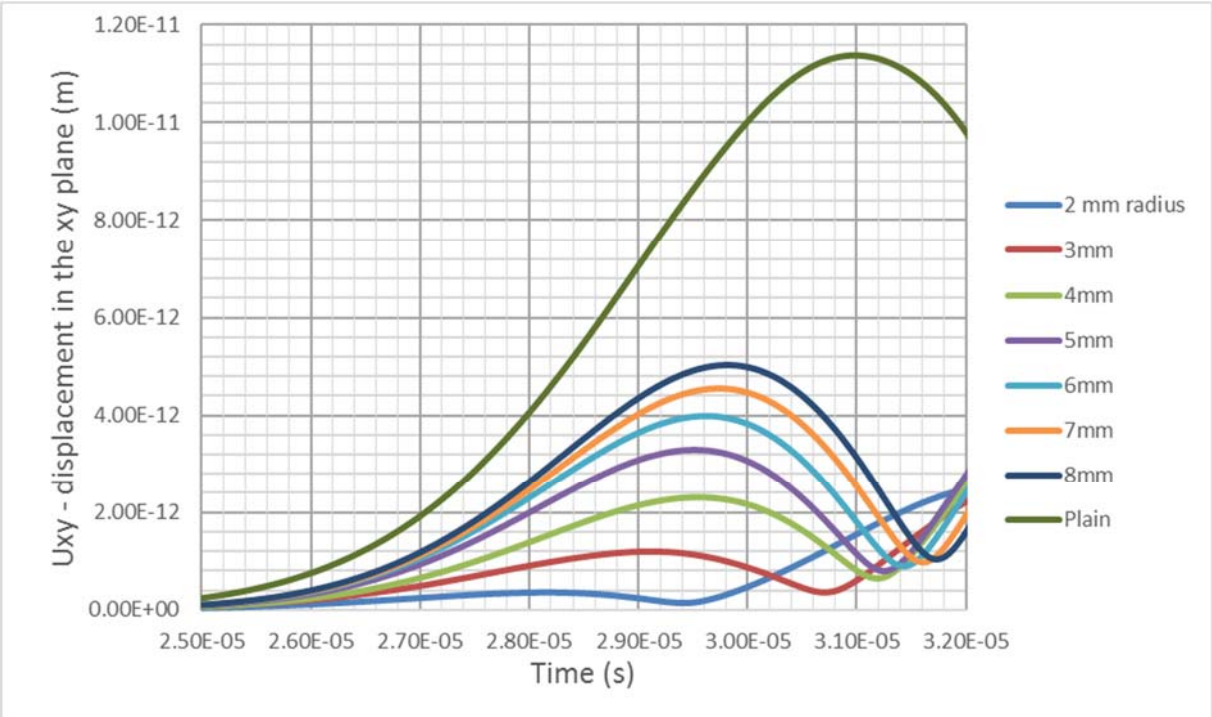

Figure 13 – First S0 wave front zoomed out.

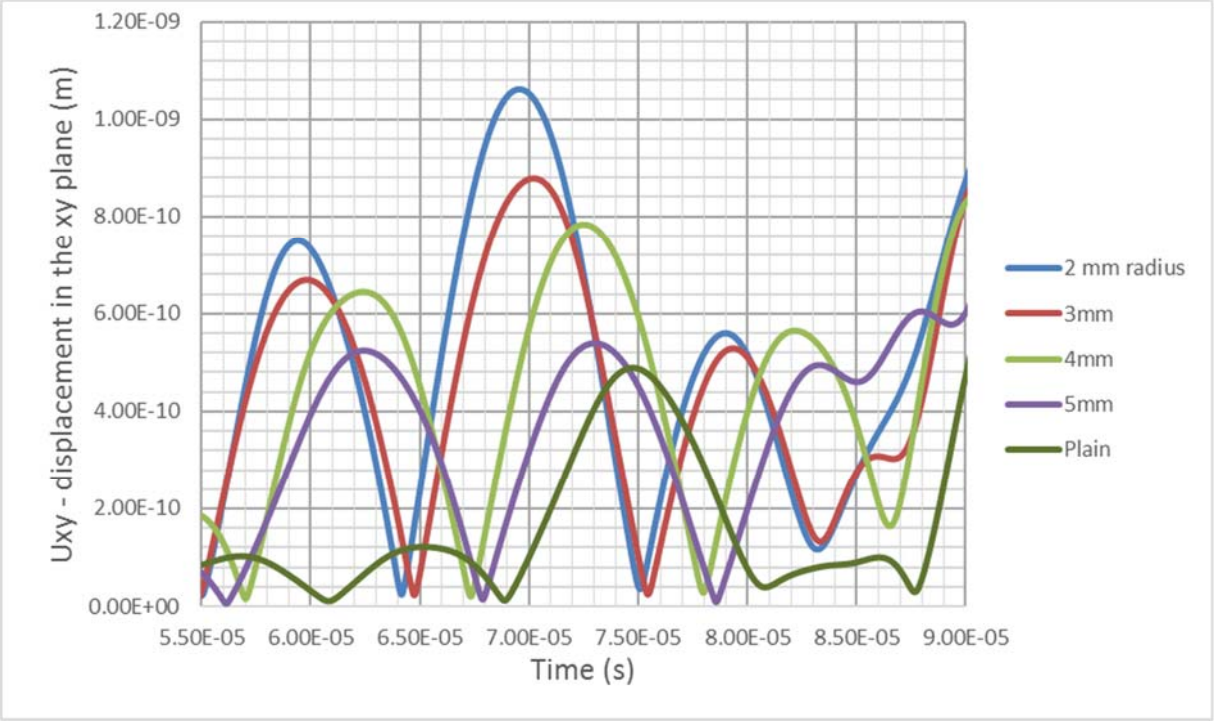

Figure 14 – A0 wave group.

In order to calculate the wave speed in the curved part, it is needed to take into account the amount of time that the wave stays in the curved part and the time it stays in the plain part, for each radius. It is assumed, as a first hypothesis, that the velocity in the plain section changes abruptly to the velocity in the curved section. Hence, with this hypothesis, it is possible to use the following equation, after the plain speed is determined and knowing the final time of flight (TOF):

$$TOF = tplain + tcurved$$

$$tplain = \frac{(c+b)}{Vplain}\ ;\ tcurved = \frac{2\cdot\alpha\cdot r}{Vcurved}\ ;\ TOF = \frac{(c+b)}{Vplain} + \frac{2\cdot\alpha\cdot r}{Vcurved}\ ,hence: \tag{4}$$

$$Vcurved = \frac{2\cdot\alpha\cdot r}{TOF - \frac{(c+b)}{Vplain}}.$$

Hence, using equation 4, table 3 is generated for S0 mode.

Table 3 – S0 velocities vs leading edge radiuses.

	Plain section		Curved section		
Radius (mm)	**Time (s)**	**S0 Velocity (m/s)**	**Time (s)**	**S0 Velocity**	**Change (%)**
2	3.100E-05	2.581E+03	2.82E-05	**-2.488E+03**	-
3	3.076E-05	2.601E+03	2.91E-05	1.195E+04	360%
4	3.081E-05	2.597E+03	2.96E-05	4.640E+03	79%
5	3.080E-05	2.597E+03	2.95E-05	4.049E+03	56%
6	3.076E-05	2.601E+03	2.96E-05	3.555E+03	37%
7	3.072E-05	2.604E+03	2.97E-05	3.241E+03	24%
8	3.080E-05	2.597E+03	2.98E-05	3.129E+03	20%
50	5.528E-05	2.713E+03	5.49E-05	2.736E+03	1%

It is possible to see from table 3 that for 2 mm radius, the calculated value of S0 velocity for the curved part is negative. That anomaly happens because the hypothesis of abrupt change of velocity doesn´t hold and is worse for smaller radiuses of the leading edge. In other words, the plain section S0 speed close to the leading edge increases smoothly. Calculating the time it would take for the wave to travel the plain part until the curved receptor (c+b) using the speed of the third column of table 3, it was found that this value would be 2.96e-5 s for 2 mm radius. That value alone is bigger than the total time of the fourth column of table 3. Hence, it is proved that the plain section velocity close to the leading edge needs to be bigger so that the wave takes a total of 2.82e-5 s to travel both the plain and the curved section.

For future studies, one might find the shape of the plain section wave speed function near the leading edge, so that better estimates of speed increase with curvature are obtained for smaller radiuses.

5 CONCLUSION

It was possible to see from the simulations, that the presence of curvature affects considerably the behavior of Lamb Waves. It was found qualitative evidence of refraction (change of speed) in the leading edge. Also, it was possible to have first estimates of S0 mode speed changes versus radiuses of the leading edge. The amplitude of the incoming wave also changed considerably, for the same source energy. It was found, also, that the change of speed is not abrupt (step) when the wave crosses the boundary between curved and plain sections. The speed of the wave increases around this boundary, for the plain section.

The speed of the waves, both S0 and A0 change sensibly depending on the propagation direction, because of the orthotropic property of the laminate.

These results will influence the SHM algorithms for damage assessment, as the considered speed for the time of flight calculations will change depending on curvature and direction.

6 ACKNOWLEDGEMENTS

The authors acknowledge the support of the Brazilian research agencies FAPEMIG (in Portuguese "Fundação de Amparo à Pesquisa do Estado de Minas Gerais"), CNPq and CAPES.

REFERENCES

[1] IEA. (2013). "Technology Roadmap - Wind Energy." s.l. : International Energy Agency.

[2] Sandia National Laboratories (2017). "Wind turbine blade cross section and structural elements". Retrieved from http://www.sandia.gov/.

[3] Wang, Y., & Zhupanska, O. I. (2015). "Lightning strike thermal damage model for glass fiber reinforced polymer matrix composites and its application to wind turbine blades". Composite Structures, 132, 1182-1191.

[4] Derriso, Mark M, et al. (2014). "Industrial Age non-destructive evaluation to Information Age structural health monitoring". Structural Health Monitoring. 2014, Vol. 13(6), pp. 591-600.

[5] Lamb, H. (1917, March). "On waves in an elastic plate". In Proceedings of the Royal Society of London A: Mathematical, Physical and Engineering Sciences (Vol. 93, No. 648, pp. 114-128). The Royal Society.

[6] Taylor, S. G., Park, G., Farinholt, K. M., & Todd, M. D. (2013). "Fatigue crack detection performance comparison in a composite wind turbine rotor blade". Structural Health Monitoring, 12(3), 252-262.

[7] Donadon L. V.; Ferreira L. P. S.; Duarte H. V. (2015). "Recent Developments in the Structural Health Monitoring in the Gravi Group in UFMG". Proceedings of the 23rd ABCM International Congress of Mechanical Engineering. COBEM.

[8] Qiu, Lei, et al. (2013). "A quantitative multidamage monitoring method for large-escale complex composite". Structural Health Monitoring. 12, 2013, Vol. 3, pp. 183 - 196

[9] Ciang, C. C., Lee, J. R., & Bang, H. J. (2008). "Structural health monitoring for a wind turbine system: a review of damage detection methods". Measurement Science and Technology, 19(12), 122001.

[10] Wang, L., & Yuan, F. G. (2007). "Group velocity and characteristic wave curves of Lamb waves in composites: Modeling and experiments". Composites science and technology, 67(7), 1370-1384.

[11] Daniel, I. M., Ishai, O., Daniel, I. M., & Daniel, I. (1994). "Engineering mechanics of composite materials". Vol. 3. New York: Oxford university press.

[12] Courant, R., Friedrichs, K., & Lewy, H. (1967). "On the partial difference equations of mathematical physics". IBM journal, 11(2), 215-234.

RESPONSIBILITY NOTICE

The authors are the only responsible for the printed material included in this paper.